




A model for galaxy-galaxy strong lensing statistics in surveys

G. Ferrami^{1,2}   J. Stuart B. Wyithe^{1,2,3} 

¹*School of Physics, University of Melbourne, Parkville, VIC 3010, Australia*

²*ARC Centre of Excellence for All-Sky Astrophysics in 3 Dimensions (ASTRO 3D)*

³*Research School of Astronomy and Astrophysics, Australian National University, Canberra, ACT 2611, Australia*

Accepted XXX. Received YYY; in original form ZZZ

ABSTRACT

Photometric wide-area observations in the next decade will be capable of detecting a large number of galaxy-scale strong gravitational lenses, increasing the gravitational lens sample size by orders of magnitude. To aid in forecasting and analysis of these surveys, we construct a flexible model based on observed distributions for the lens and source properties and test it on the results of past lens searches, including SL2S, SuGOHI and searches on the COSMOS HST and DES fields. We use this model to estimate the expected yields of some current and planned surveys, including Euclid Wide, Vera Rubin LSST, and Roman High Latitude Wide Area. The model proposed includes a set of free parameters to constrain on the identifiability of a lens in an image, allowing construction of prior probability distributions for different lens detection methods. The code used in this work is made publicly available.

Key words: gravitational lensing: strong – galaxies: high-redshift – galaxies: evolution

1 INTRODUCTION

Strong gravitational lensing is a powerful probe of both astrophysics and cosmology, as its effects depend on the surface mass density of the lens and the cosmological distances between the observer, lens and source. Strong lensing has been used to study the inner structure of galaxies (e.g., Zwicky 1937, Treu & Koopmans 2002, Koopmans & Treu 2003) and their evolution with cosmic time (e.g., Grillo et al. 2009, Sonnenfeld et al. 2013b, Etherington et al. 2023, Tan et al. 2023), as well as to constrain the dark matter fraction in massive ETGs (e.g., Grillo 2010, Sonnenfeld et al. 2015), their stellar initial mass function (IMF, e.g., Treu et al. 2010, Smith et al. 2015, Sonnenfeld et al. 2019) and the presence of substructures within them and along their line-of-sight (e.g., Mao & Schneider 1998, Vegetti et al. 2010, Oldham & Auger 2018, Despali et al. 2018). Galaxy scale strong lenses have been used to study the high redshift quasar luminosity function (e.g., Turner et al. 1984, Webster 1991, Wyithe & Loeb 2002a) and galaxy luminosity function, especially its bright end (e.g., Wyithe et al. 2011, Barone-Nugent et al. 2015, Mason et al. 2015, Ferrami & Wyithe 2023). Lensing can also be a tool to measure the values of cosmological parameters independently from the distance ladder, from either observation of time-delay between multiple images of the same source (e.g., Refsdal 1964, Suyu et al. 2017, Wong et al. 2020, Birrer et al. 2020, Shajib et al. 2023), joint strong lensing and dynamical analysis (e.g., Grillo et al. 2008), lenses with multiple source planes (e.g., Gavazzi et al. 2008, Collett & Auger 2014), or from source and deflector populations (e.g., Oguri et al. 2012). On kiloparsec scales, strong gravitational lensing, in combination with stellar kinematics of the lens, is sensitive to the weak-field metric of gravity and can be used as a test for General Relativity (e.g., Schwab

et al. 2010, Collett et al. 2018). For many of these analyses, the small sample size dominates the statistical uncertainty. A large sample of lenses with sources at different redshifts is critical to marginalise over any trends in the redshift evolution of the deflector population and would unlock a broader range of investigations accessible with greater statistical power. However, galaxy scale lenses are difficult to observe, as they require alignment within $\sim 1''$ of a light source and a foreground object with a sufficiently large surface mass density, along with deep and high-resolution observations of a large fraction of the sky to identify rare cases.

Since the first strong lens was discovered (Q0957+561; Walsh et al. 1979), a combination of serendipitous discoveries and systematic searches made the number of known galaxy-scale lenses steadily increase: 11 in the early 1990s (Blandford & Narayan 1992), around 200 in 2010 (Treu 2010), and $O(10^3)$ galaxy-scale lenses found to date¹ (e.g., Sonnenfeld et al. 2020). During the next decade, $O(10^5)$ strong lenses (Collett 2015, Marshall et al. 2005, Holloway et al. 2023b) will be discovered by wide-field photometric surveys offering improved depth, area, and resolution compared to existing data. These include the Euclid Wide survey (Euclid Collaboration et al. 2022), Vera Rubin Observatory LSST (Ivezic et al. 2008), and Roman Space Telescope High Latitude Wide Area Survey (Spergel et al. 2015).

Spectroscopic follow-up of a candidate lens is necessary for two reasons: first to distinguish morphological features that appear similar to strong lenses (e.g., ring galaxies, star forming tidal streams) from genuine galaxy scale lenses, and second to convert the angular quantities of the putative lenses into physical units. The 4MOST Strong Lensing Spectroscopic Legacy Survey (4SLSLS, Collett et al.

¹ The exact number depends on the cut in purity applied to the sample, as many of these lenses have high probability of being lenses, but no spectroscopic confirmation.

* E-mail: gferrami@student.unimelb.edu.au

2023) will provide spectroscopic redshifts for $O(10^4)$ lens-sources pairs, and velocity dispersion measurements for ~ 5000 lenses.

Such large samples of strong lenses will unlock considerable scientific potential through vastly improved statistics (e.g. [Sonnenfeld & Cautun 2021](#); [Sonnenfeld 2022a](#), [Sonnenfeld 2022b](#)). To tackle the forthcoming thousand-fold increase in data volume, model inference must be automated, and made robust without human intervention (e.g., `PYAUTOLENS` [Nightingale & Dye 2015](#), [Etherington et al. 2022](#); or `DOLPHIN` [Shajib et al. 2021](#)).

Many methods have been used to find galaxy scale strong lenses, mostly from photometric datasets. These techniques include feature detection algorithms (e.g., `ARCFINDER`, [Alard 2006](#), [More et al. 2012](#); `RINGFINDER`, [Gavazzi et al. 2014](#); `OF BNA`, [Diehl et al. 2017](#), [O'Donnell et al. 2022](#)); lens model fitting algorithms (e.g. [Marshall et al. 2009](#), [Chan et al. 2015](#)); a combination of the previous two (e.g., `YATTALENS`, [Sonnenfeld et al. 2018](#)); principal component analysis to subtract galaxies from imaging data (e.g., [Joseph et al. 2014](#)); visual search by researchers ([Hogg et al. 1996](#), [Moustakas et al. 2007](#), [Faure et al. 2008](#), [Pawase et al. 2014](#)); citizen science ([Marshall et al. 2016](#); [More et al. 2016](#); [Sonnenfeld et al. 2020](#)). Recently, machine learning has been commonly used as a new tool. Some of the most common architectures employed so far in lens searches are Convolutional Neural Networks (CNNs, see for example [Jacobs et al. 2017](#), [Jacobs et al. 2019b](#), [He et al. 2020](#), [Stein et al. 2022](#), [Angora et al. 2023](#), [Euclid Collaboration et al. 2023](#)), Support Vector Machines (SVM, e.g., [Hartley et al. 2017](#)) and self-attention encoding (e.g., [Thuruthipilly et al. 2022](#)). Note that the techniques listed above can be combined to classify a lens sample (e.g., an ensemble classifier based on neural network and citizen science lens finders in [Holloway et al. 2023a](#)).

Given a certain intrinsic distribution in redshift and mass of lenses, any given search measures the distribution of lensed sources *identifiable* given the observational constraints which could be then biased by the telescope in use and the adopted search method. In general, it is non-trivial to infer the intrinsic distribution of lenses given the observed one (e.g., [Sonnenfeld et al. 2023](#)). Past efforts to characterize the intrinsic distribution of identifiable lenses for a given survey include analytical models for lensing statistics of bright galaxies in spectroscopic searches ([Serjeant 2014](#)) and AGNs and supernovae in photometric surveys ([Oguri & Marshall 2010](#)), and simulation-based models for lensing statistics of galaxy-galaxy lensing ([Collett 2015](#), [Holloway et al. 2023b](#)).

In this paper we present a flexible analytic model to forecast the expected yields of some current and planned surveys using fiducial distributions for the lens and source properties as constrained by observations. The model proposed includes a set of free parameters to explicitly set the constraints on the identifiability of a lens in an image, considering both the cases where the lens light can and cannot be subtracted. This paper is organized as follows. In Section 2, we introduce the model for galaxy scale strong lens statistics. In Section 3, we consider the response of our model to variations in its input parameters. In Section 4, we compare our model results to some past strong lens search samples. In Section 5, we present forecasts for the number of strong lenses in ongoing and future surveys. In Section 6, we estimate the fraction of rare quad configurations and dual-plane lenses. In Section 7, we discuss potential improvements to the lens and source population models, and their effect on extreme lens configurations (i.e., sources at high redshift and/or highly magnified). Conclusions are presented in Section 8. Throughout this paper, we adopt $H_0 = 70 \text{ km s}^{-1} \text{ Mpc}^{-1}$, $\Omega_0 = 0.3$, $\Omega_\Lambda = 0.7$.

2 A MODEL FOR GALAXY-GALAXY LENSES STATISTICS

In this paper, we present a model for the statistics of galaxy-galaxy lenses. Our model considers only information contained in a single photometric band. We first calculate the total number of lensed galaxies in a given patch of sky. Then we construct a flexible tool to estimate the number of *identifiable* lensed sources. Initially, we assume that the lens light can be completely subtracted. We then relax this condition to account for the effect of lens light.

2.1 Lensing probability and Magnification Bias

The *a-priori* probability for a source to be lensed by a foreground galaxy into multiple images is defined as the multiple image optical depth τ ([Turner et al. 1984](#)), calculated as the integral of the lensing cross section over the lens population and redshift. Under the usual approximation that the population of lenses is dominated by early-type galaxies (e.g., [Turner et al. 1984](#), [Kochanek 1996](#), [Oguri & Marshall 2010](#)), we take the mass distribution profile of the lenses to be a Singular Isothermal Ellipsoids (SIE), which has been shown to be a very reliable approximation for the total matter surface density profile at the radial scales relevant for galaxy-galaxy lensing ([Gavazzi et al. 2007](#), [Koopmans et al. 2009](#), [Lapi et al. 2012](#), [Sonnenfeld et al. 2013b](#)).

The strong lensing magnification effects of SIE lenses averaged over the possible source positions, depend only on the velocity dispersion σ of the stellar component (a proxy for the total mass) and on the ellipticity of the SIE mass distribution. We can calculate τ for a population of sources at redshift z_s given by the lenses intervening on the line-of-sight at each redshift $z_l < z_s$ as

$$\tau(z_s) = C \int_0^{z_s} dz_l \int_0^\infty d\sigma \Phi(\sigma, z_l) (1 + z_l)^3 \frac{cdt}{dz_l} \pi D_l^2 \theta_E^2(\sigma, z_l); \quad (1)$$

where C is a lens model dependent constant ($C = 1$ for a singular isothermal sphere, $C < 1$ for a singular isothermal ellipsoid lens), $\Phi(\sigma, z_l)$ is the velocity dispersion function (VDF) of early-type galaxies, D_l is the angular diameter distance of the lens and θ_E is its Einstein radius. We adopt the [Mason et al. \(2015\)](#) velocity dispersion function and its evolution with redshift $\Phi(\sigma, z_l)$ with their best-fit values for the relevant parameters. In the next Sections, we will explore two other VDFs: the local Velocity Dispersion Function measured by SDSS ([Choi et al. 2007](#)), and the distribution calibrated on a sample of strong lenses ([Geng et al. 2021](#)). We included the dependency on the ellipticity distribution of lenses using the geometry constraints up to $z = 2$ provided by the SDSS ([van der Wel et al. 2014](#)), following the same method used in [Ferrami & Wyithe \(2023\)](#). Averaging over the observed early-type galaxies ellipticity distribution, we find $C \approx 0.9$.

The luminosity function (LF) describes the comoving density of galaxies with magnitude between M and $M + dM$. The LF is often approximated by a Schechter profile

$$\Psi(L)dL = \Psi_\star \left(\frac{L}{L_\star}\right)^\alpha \exp\left(-\frac{L}{L_\star}\right) \frac{dL}{L_\star}, \quad (2)$$

and the parameters Ψ_\star , α , L_\star evolve with redshift. We adopt the rest frame UV LF evolution presented in [Bouwens et al. \(2022\)](#) for $z \leq 9$. Strong lensing can produce an apparent magnification of the source, which in turn alters the observed luminosity function of high redshift sources (e.g., [Turner et al. 1984](#), [Pei 1995](#), [Wyithe et al. 2011](#)). The

lensing bias B quantifies the excess of lensed sources of magnitude M at redshift z_s is

$$B(M, z_s) = \frac{1}{\Psi(M, z_s)} \int_0^\infty \frac{d\mu}{\mu} \frac{dP}{d\mu} \Psi \left(M + \frac{5}{2} \log(\mu), z_s \right). \quad (3)$$

Here $\Psi(M, z_s)$ is the unlensed galaxy luminosity function and $\frac{dP}{d\mu}$ represents the magnification distribution of the brightest image produced by a lens with isothermal mass distribution. Following the finding of Ferrami & Wyithe (2023) that source size only affects magnification bias for the brightest galaxies, in this paper we do not account for the effect of source size in the magnification bias, since the main contribution to the observed lens numbers comes from its faint end. The difference between the observed flux in a given bandpass and the rest frame magnitude given by the UV LF is determined by the galaxy spectral energy distribution (SED) and the bandpass profile. The apparent luminosity of a galaxy at redshift z observed in a bandpass b is related to absolute UV magnitude as

$$m_b = M_{UV} + DM(z) + K_{UV,b}(z), \quad (4)$$

where $DM(z)$ is the cosmological distance modulus and $K_{UV,b}(z)$ is the K-correction.

In this work, we approximate the K-correction from the UV continuum slope β ($f_\lambda \propto \lambda^\beta$) of a star-forming galaxy SED. Calibrating the SED continuum slope from the observations accounts for the effects of dust attenuation in the galaxy rest frame. For sources with redshift in the range $0 < z_s < 4$ we adopt the linear fit $\beta = -1.5 - 0.12(z_s - 1)$ over the magnitude range $-19 < M_{UV} < -20$ shown in Mondal et al. (2023). For the source redshift range $4 \leq z \leq 10$, we adopt the piecewise linear relations between β and M_{UV} studied Bouwens et al. (2014) (see also Sect. 2.3 of Liu et al. 2016 for a detailed implementation of these relations).

2.2 Total lensed background

For a lens with fixed velocity dispersion σ and redshift z_l , the number density of background sources with absolute magnitude M at redshift z_s it lenses is obtained as the product between the luminosity function and the comoving volume behind this single lens (enclosed in the portion of the source plane that can produce multiple images). In a flat universe, this equates to

$$\frac{dN_{SL}(M, z_s | \sigma, z_l)}{dz_s dM} = C \pi \theta_E^2 D_c^2(z_s) \frac{c}{H(z_s)} \Psi(M, z_s) B(M, z_s), \quad (5)$$

where D_c is the comoving distance to the source.

Assuming a survey with area A_s in square degrees, integration over the lens population and redshift and the source magnitude and redshift gives the total number of lensed sources in a given field,

$$N = \int_0^{z_{s,max}} dz_s \int_0^{M_{cut}(z_s)} dM \int_0^{z_s} dz_l \int_0^\infty d\sigma \frac{dV(A_s, z_l)}{dz_l} \times \frac{dN_{SL}(M, z_s | \sigma, z_l)}{dz_s dM} \Phi(\sigma, z_l), \quad (6)$$

where $z_{s,max}$ is the maximum redshift considered for the source population, $M_{cut}(z_s)$ is the magnitude cut² applied the survey data m_{cut} corrected for the distance modulus, K-correction, and $\frac{dV}{dz_l}$ is the section of the comoving volume shell behind A_s .

Note that by construction Eq. 5 accounts only for the region behind a lens that produces multiple images (i.e., a magnification ≥ 2 for a SIE lens).

² In general, m_{cut} is chosen to be fainter than the survey magnitude limit m_{lim} to obtain higher completeness in the sample.

2.3 Detecting arcs and counterimages

In lens searches the identification of a lens can also be through features, such as extended arcs where a second image is not detected, or two or more images with the same colour detected around $\approx 1''$ around the candidate lens. In this section, we derive an analytical model that accounts for the minimum magnification of the brightest image (i.e. minimum tangential stretch of an arc) and the apparent luminosity of a counterimage.

Assuming $B = 1$ outside τ , the lensed fraction for a given source magnitude and redshift is

$$F_{lens}(M, z_s) = \frac{\tau B(M, z_s)}{\tau B(M, z_s) + (1 - \tau)}. \quad (7)$$

The fraction of lenses with a magnification greater than some value μ_a is then

$$\frac{F_{arc}(\mu > \mu_a)}{F_{lens}} = \frac{\int_{\mu_a}^\infty \frac{d\mu}{\mu} \frac{dP}{d\mu} \Psi \left(M + \frac{5}{2} \log(\mu), z_s \right)}{\int_{\mu_{min}}^\infty \frac{d\mu}{\mu} \frac{dP}{d\mu} \Psi \left(M + \frac{5}{2} \log(\mu), z_s \right)}, \quad (8)$$

where μ_{min} is the lowest possible magnification for the brightest image in the multiple image regime. Similarly, the fraction of lenses with the luminosity of the n -th image of a SIE lens above the magnitude limit is

$$\frac{F_{nth}(M_n > M_{lim})}{F_{lens}} = \frac{\int_{\mu_{n,L}}^{\mu_{n,U}} \frac{d\mu}{\mu} \frac{dP}{d\mu} A_n \Psi \left(M + \frac{5}{2} \log(\mu), z_s \right)}{\int_{\mu_{min}}^\infty \frac{d\mu}{\mu} \frac{dP}{d\mu} \Psi \left(M + \frac{5}{2} \log(\mu), z_s \right)}, \quad (9)$$

where $\mu_{n,L}$ and $\mu_{n,U}$ are respectively the lower and upper magnification limit for the brightest image that corresponds to a magnification of the n -th image high enough to be brighter than the survey's flux limit. The fraction F_n is properly normalised by A_n , which is the portion of the area within the outermost caustic that can produce a n -th image. In a SIS lens, there is an analytical relation between the magnification of the first and second images ($\mu_2 = \mu_1 - 2$) and therefore getting F_{2nd}^{SIS} is straightforward. Since such an analytical solution is not available for a generic SIE model, we compute an effective relation between the magnification of the primary image and the magnification of the second, third (in the naked cusp regime), and fourth image. To do so, we first compute the magnification distribution functions for the four images of a SIE as a function of the lens ellipticity. Then we map those functions into each other through an integral relation ($\int_{-\infty}^{\mu_1} \frac{dP}{d\mu_1} d\mu = \int_{-\infty}^{\mu_n} \frac{dP}{d\mu_n} d\mu$) and use that to implicitly solve for the equation $\log(\mu_n/\mu_1) = 0.4(M_1 - M_{lim})$. In Figure 1 we plot such lens fraction statistics as a function of the magnitude of the primary image and the source redshift.

Accounting for the identification of arcs and counterimages introduces a correction to Eq. 5. We specifically introduce a factor of $\mathcal{F}_{arc} = F_{arc}/F_{lens}$ and $\mathcal{F}_{nth} = F_{nth}/F_{lens}$ as so far we were considering all the sources within the outer caustic.

2.4 Selection on minimum SNR and angular size

The possibility of detecting a galaxy also depends on the ability to collect enough of its photons to overcome the noise in the detector. This imposes a minimum Signal-to-Noise Ratio (SNR) that constrains the number of *identifiable* lenses. In the same way, the angular size of the lensed images must be resolved in order to identify a lens. This requires the Einstein radius to be larger than the seeing or PSF of a given survey.

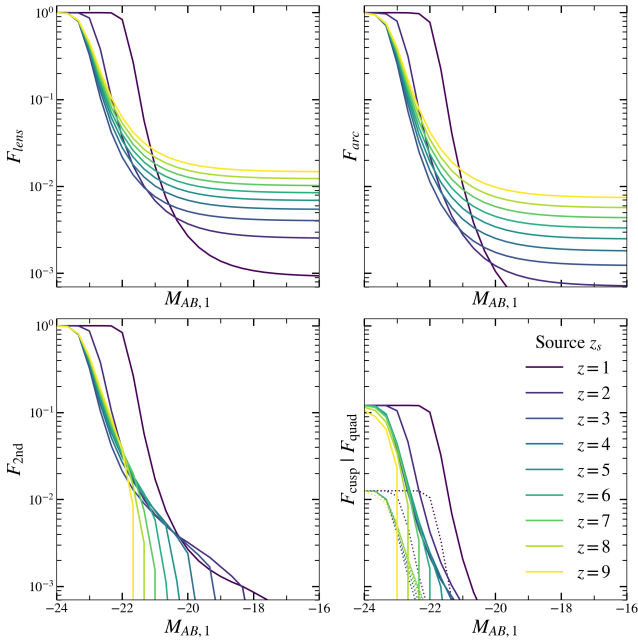


Figure 1. Fraction of lensed objects (top left) as a function of source redshift and absolute UV magnitude. The top left panel shows the fraction of multiply imaged sources (see Eq. 7), while the top right panel contains the profile for the fraction of sources imaged into an arc stretched by at least a factor of 3 (Eq. 8). The bottom panels show the fraction of second images (left) and third/fourth images in a cusp/quad configuration (right) above an apparent limit magnitude of $m_{\text{lim}} = 28.5$.

2.4.1 Signal-to-noise ratio

For a given detector, the number of photons from a source of apparent magnitude m_b is

$$N_\gamma = t_{\text{exp}} 10^{\left(\frac{ZP - m_b}{2.5}\right)}, \quad (10)$$

where the zero point ZP is the magnitude of an object that produces one count per second and t_{exp} is the total exposure time of the survey. Since we do not have a set of pixels to evaluate the individual contribution to the SNR, we approximate it over the apparent size of the source in the sky as

$$\text{SNR} = \frac{N_\gamma}{\sqrt{N_\gamma + \sigma_{\text{sky}}^2}}, \quad (11)$$

where $\sigma_{\text{sky}}^2 = N_{\text{sky}} \pi \vartheta_e^2$ is the survey background noise. N_{sky} is the background photon count per steradian, obtained from the sky background magnitude m_{sky} as in Eq. 10, and the effective radius in radians ϑ_e comes from the luminosity-size relation, calculated on the intrinsic UV magnitude. We use the $M_{UV} - r_e$ relation evolution with redshift presented in Shibuya et al. (2015):

$$r_e = r_0 \left(\frac{L_{UV}}{L_0}\right)^\alpha, \quad \left[\alpha = 0.27, r_0 = 6.9(1+z)^{-1.2} \text{ kpc}\right] \quad (12)$$

where r_0 value represents the effective radius expressed in kpc at a luminosity of L_0 corresponding to $M_{UV} = -21$. We can then evaluate the SNR₁ (SNR₂) for the brightest (secondary) image in a lens knowing that its average magnification in a SIS lens is $\bar{\mu}_1 = 3$ ($\bar{\mu}_2 = 1$). We can now define two selection functions $\mathcal{S}_{1/2} = H(\text{SNR}_{1/2} > \text{SNR}_{\text{min}})$, where H is the Heaviside step function,

imposing a cut-off for the lenses that have the first or second image below a minimum value of SNR.

2.4.2 Einstein radius vs. seeing / PSF

In a lens galaxy, the multiple images appear at an angular scale of the order of the Einstein radius Θ_E . For a lens to be identifiable, the background images must be resolved, i.e. the Einstein radius must be bigger than the seeing (or PSF) of the observations. We define a Heaviside selection function $\mathcal{S}_E = H(\theta_E > \xi s)$, excluding the lenses with an Einstein radius smaller than ξ times the seeing s .

2.5 Number of lenses with lens light subtracted

We can use the expressions for the fraction of lenses with a clear arc and/or with the second brightest image above the flux limit derived in Eqs. 8-9 as a weighting to evaluate the number of the *detectable* lensed sources in the background of a given lens,

$$\frac{dN_{SL}^{obs}}{dz_s dM}(M, z_s, \mu_a, M_{\text{lim}}) = \frac{dN_{SL}}{dz_s dM} \times \max(\mathcal{S}_1 \mathcal{F}_{\text{arc}}, \mathcal{S}_2 \mathcal{F}_{2\text{nd}}) \mathcal{S}_E, \quad (13)$$

where the selection functions $\mathcal{S}_{1/2}$ and \mathcal{S}_E have been defined in the previous Section. This constraint should give the bulk of the identifiable lenses, even though for ground-based surveys (i.e. large seeing) it does not retrieve the (small) portion of lenses that can be resolved after deconvolving the PSF. The maximum $\max(\mathcal{F}_{\text{arc}}, \mathcal{F}_{2\text{nd}})$ approximates the detection selection up to a factor of order 2 in the luminosity interval where $\mathcal{F}_{\text{arc}} \approx \mathcal{F}_{2\text{nd}}$.

Substituting N_{SL}^{obs} to N_{SL} in Eq. 6 gives the number of lensed sources at redshift z_s with magnitude M detectable by a given survey, assuming that the lens light can be removed without loss of information.

2.6 Accounting for the lens light profile

In previous sections, we calculated the number of gal-gal lenses in a survey in which the lens light is assumed to be completely removed so that the limiting factors in the observability of a lensed image are flux limit and seeing of a specific survey.

We now consider lens galaxies in which the lens light has not been subtracted. Such lens systems may prove difficult to identify, especially for bright lenses (favoured in the lens statistics as they often are massive, i.e. good deflectors) and for faint sources (e.g., Kochanek 1996; Wyithe & Loeb 2002b). We can introduce the effect of the lens light profile in our model by comparing the surface brightness (SB) of the source (a conserved quantity in lensing) to the SB of the lens galaxy, evaluated at the position of the multiple images.

To do so, we will use the Fundamental Plane relation for early-type galaxies (Djorgovski & Davis 1987, Dressler et al. 1987, see also Treu et al. 2001):

$$\log R_e = \alpha \log_{10} \sigma_0 + \beta \langle \mu_e \rangle + \gamma, \quad (14)$$

where R_e is the effective radius, σ_0 is the central velocity dispersion and $\langle \mu_e \rangle$ is the mean surface brightness measured within the effective radius. The FP parameters in the *grizYJHK* wavebands are taken from La Barbera et al. (2010b). The evolution with lens redshift of the three parameters is given by a linear interpolation between redshift $z = 0$ and $z = 2$ in the B-band (Stockmann et al. 2021, see Table 2). We further assume that the FP parameters evolve with the same slope in every rest-frame wavelength.

To account for the lens light profile, we obtain the surface brightness sampling the Fundamental Plane for a given $\sigma_0 = \sigma$ and a log-gaussian distribution of effective radii with mean and variance that depends on the lens rest frame emission waveband as described in La Barbera et al. (2010a) (see in particular Fig. 11 of that paper), with the mean evolving with redshift following the same trend as the scale-radius in the $M_{UV} - R_e$ relation from Shibuya et al. (2015) (see Sect. 2.4).

The parameters of the FP are taken from the lens rest-frame waveband that would be redshifted to observing waveband b , to be specified for each survey. We then consider a deVaucouleur profile (de Vaucouleurs 1948, de Vaucouleurs 1953) for the SB of the lens and evaluate it at the position of the bright and secondary images, and compare it with the SB of the source (accounting for cosmological dimming). To obtain a simple analytical form for the position of the bright and secondary images, we model the lens mass density as a Singular Isothermal Sphere (SIS). In a SIS lens, the distance between the first and second image is always $\Delta\theta = 1\theta_E$, and the position of the brightest image is uniformly distributed between $\theta_E < \theta_1 < 2\theta_E$.

We calculate the surface brightness of a source of magnitude m_b using the $M_{UV} - R_e$ relation from Shibuya et al. (2015) introduced in Sect. 2.4. We then include the probabilities of seeing the first and second image through the lens light, P_1^{LL} and P_2^{LL} , into Eq. 13 as

$$\frac{dN_{SL}^{obs,LL}}{dz_s dM} (M, z_s, \mu_a, M_{lim}, b) = \frac{dN_{SL}}{dz_s dM} \times \max(\mathcal{S}_1 \mathcal{F}_{arc} P_1^{LL}, \mathcal{S}_2 \mathcal{F}_{2nd} P_2^{LL}) \mathcal{S}_E. \quad (15)$$

Substituting $N_{SL}^{obs,LL}$ to N_{SL} in Eq. 6 gives the number of lensed sources at redshift z_s with magnitude M detectable by a given survey without removing the lens light.

This approach provides a lower bound on the number of observable lenses, as colour information from observations in multiple photometric bands of the same field can yield higher fractions of detected lenses than this method based on the SB alone.³ On the other hand, the model without lens light introduced in the previous section provides an upper bound on the number of identifiable lenses. The combination of these two estimates could provide some insight into the response of the completeness function on the survey characteristics.

Table 1 summarizes the input parameters and distributions that enter in our model. For an example of the output of the model based on the Euclid Wide VIS band, see Fig. 2. The figure shows the projections of the lens number density over the parameter space of redshifts and velocity dispersion (z_l, z_s and σ).

3 MODEL RESPONSE TO INPUT PARAMETERS

The main advantage of an analytic model over a simulation-based approach is the ability to vary all the input parameters and fiducial distributions at little computational cost. In this section, we discuss how different assumptions on the lens population and some of the model input parameters listed in Table 1 influence the predicted lens and source distribution in mass and redshift, as well as the total number of lenses forecast by the model.

As an illustration Fig. 3 shows the predicted distributions of lens

³ For background galaxies hosting an active AGN or a supernova event, luminosity time variation accessible by cadenced surveys can also increase the fraction of identifiable lensed sources.

Table 1. Summary of parameters and functions that constitute the input of our model. When values are indicated, these are used throughout the paper. Otherwise, the values indicated with a dash are survey-dependent (they can be found in Tables 2 - 4). The value of μ_{arc} , ξ , and SNR_{min} are chosen to match the lens identifiability prescriptions adopted in Collett 2015 and Holloway et al. 2023b.

Parameter	Value	Description
μ_{arc}	3	Minimum magnification of bright image
ξ	1.5	Seeing threshold factor
SNR_{min}	20	Minimum SNR for lens detection
m_{lim}	-	5σ magnitude limit of the survey
m_{cut}	-	Cut in magnitude
A_S	-	Survey area in square degrees
s	-	Seeing in arcsec
b	-	Observing photometric band
ZP	-	Survey zero point in the band b
t_{exp}	-	Total exposure time
m_{sky}	-	Sky background magnitude
Functions	Ref	
SIE	1	Lens total mass profile
$\Psi(L, z)dL$	2	Source UV Luminosity function
$M_{UV}-R_e$	3	Luminosity size relation
$\Phi(\sigma, z)$	4, 5	Velocity dispersion function
Ell. Distr.	6	Lens ellipticity distribution
FP	7	Fundamental plane parameters

Notes. ¹Kormann et al. (1994), ²Bouwens et al. (2022), ³Shibuya et al. (2015), ⁴Mason et al. (2015), ⁵Geng et al. (2021), ⁶van der Wel et al. (2014), ⁷La Barbera et al. (2010b)

Table 2. Survey zero-points used for the lens frequency estimates and value for the uniform sky background. For the Roman telescope, we use the same value inferred from the filter transmission curves by Holloway et al. 2023b.

Telescope	Filter	ZP [mag]	m_{sky}	Ref
HST	F814W	25.95	20	1
	F115W	27.59	22	
JWST	F150W	27.89	22	2 and 3
	F277W	27.98	22	
CHFT	i	26.24	19.2	4
DECam	i	30	20.1	4
SUBARU HSC	i	30	19.2	4
	VIS	25.50	22.2	4
EUCLID	Y	25.04	22	
	J	25.26	22	5
	H	25.21	22	
Roman	J129	26.40	22	6
Vera Rubin	i	30	20.1	7

Notes. ¹<https://acszeropoints.stsci.edu/>, ²<https://jwst-docs.stsci.edu/jwst-near-infrared-camera/nircam-performance/nircam-absolute-flux-calibration-and-zeropoints>, ³Windhorst et al. (2023), ⁴same values used in Collett (2015), ⁵Euclid Collaboration et al. (2022), ⁶Spergel et al. 2015, ⁷Ivezić et al. 2019.

system properties for EUCLID using three VDFs: the model by Mason et al. (2015), a constant VDF calibrated in the local universe from Choi et al. (2007), and the VDF inferred from a sample of gravitational lenses up to $z \sim 1$ presented in Geng et al. (2021). As expected we see that the lens velocity dispersion and redshift distributions are very sensitive to the choice of VDF, with our fiducial model producing a narrower $\frac{dP}{dz}$ peaking at a lower redshift compared

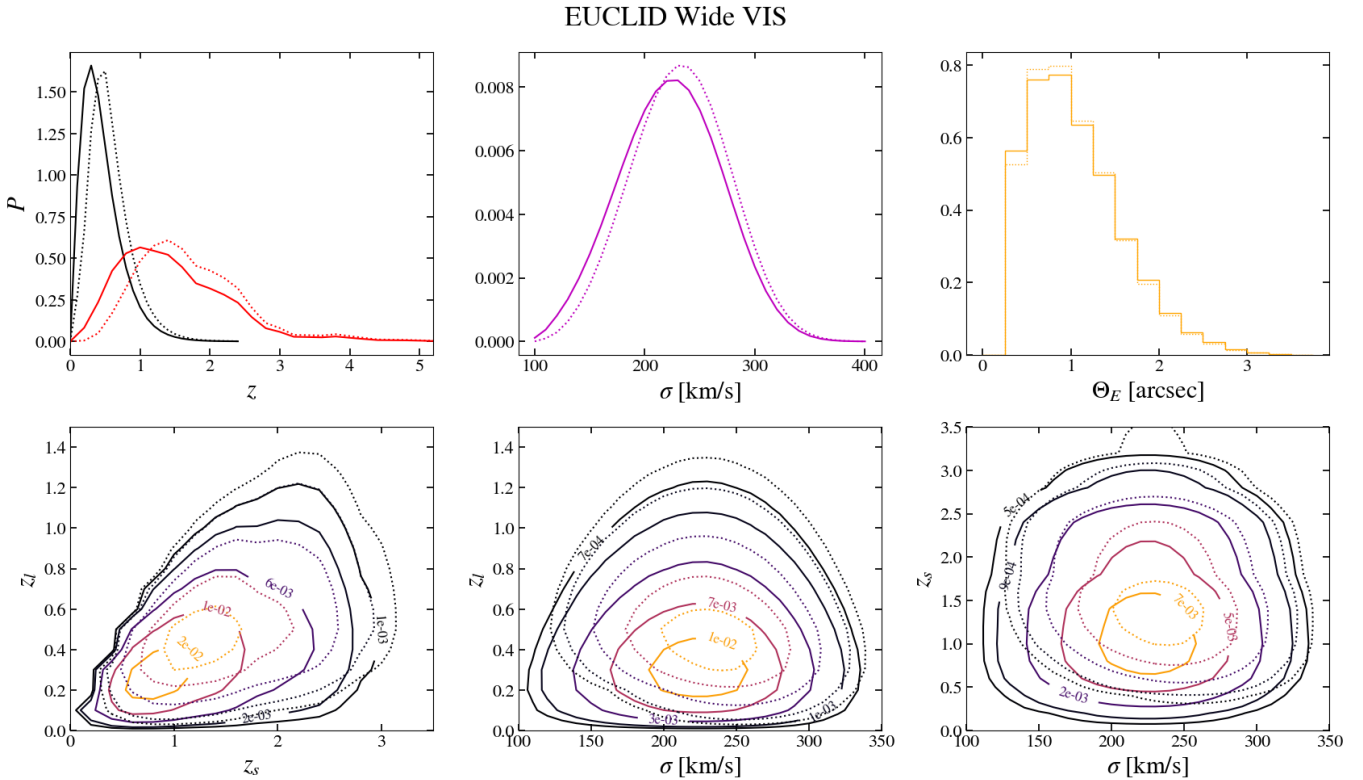


Figure 2. Statistical properties of the lens-source populations our model predicts for EUCLID Wide VIS. The plot shows the distributions assuming lens light can be completely removed (solid lines) and accounting for lens light (dotted lines). The top right panel shows the redshift distributions of the lens (red) and source (black) populations. The middle and right upper panels show the velocity dispersion and the Einstein radius distributions, respectively. The bottom row panels show how the z_l , z_s and σ distributions are linked, representing their pairwise contour plots.

to the other two VDFs considered. The distribution of Einstein ring sizes changes accordingly.

We summarize the effect of imposing a magnitude cut in Fig. 4. With decreasing m_{cut} (i.e., requiring brighter images), the number of lenses decreases smoothly (the rate at which it decreases changes depending on the survey parameters and value of apparent magnitude), while the source redshift distribution becomes skewed to lower redshift (since the distance modulus shifts more distant sources outside the range of visible magnitudes). This drives a bias to lower redshifts in the lens population, while not affecting the velocity dispersion distribution.⁴

Fig. 5 shows that the effect of seeing (or PSF) is negligible as long as it is much smaller than the typical size of the Einstein ring in arcsec. When the two angular quantities become comparable, the survey statistics degrade rapidly, favouring the more massive galaxies (i.e., biasing towards large values of velocity dispersion), and shifting lens and source redshift in opposite directions to maximize the ratio of cosmological distances D_{l_s}/D_s . This is completely degenerate with the seeing threshold factor ξ . Finally, increasing the value of the minimum magnitude of the brightest arc necessary to identify a lens decreases the number of discoverable lenses, while mildly biasing the source redshift distribution, as presented in Fig. 6.

⁴ Changing the limiting magnitude m_{lim} would have very similar effects, though it is not completely degenerate with m_{cut} as the first enters in the observable fraction of second images in Eq. 9, while the second gives the integration upper limit over magnitude in Eq. 6.

4 TESTING AGAINST OBSERVED LENS SAMPLES

In this section, we compare our results to three well-studied lens samples, each obtained with a different lens search technique: the lens catalogue obtained from a targeted visual search in the COSMOS HST field presented in Faure et al. (2008); the Strong Lensing Legacy Survey (SL2S, Cabanac et al. 2007) using the final sample presented in Sonnenfeld et al. (2013b); the CNN-based search in the DES catalogue from Jacobs et al. (2019a); and the Survey of Gravitationally-lensed Objects in HSC Imaging (SuGOHI, Sonnenfeld et al. 2018).

The summary of the results is listed in Table 3.

4.1 COSMOS HST

The Hubble Space Telescope COSMOS survey (Scoville et al. 2007) observed 1.64 deg^2 of sky in the I814W band. In Fig. 7 we compare the lens statistics predicted by our model for this field to the catalogue of lenses found in COSMOS HST through visual inspection by Faure et al. (2008). After an initial cut in magnitude to maximize completeness ($m_{I814W} < 25$), their observational catalogue was built in four steps: select potential lenses among bright ($M_V < -20$) foreground ($0.2 < z_{\text{phot}} < 1$) ETGs, inspecting $10'' \times 10''$ cutouts around the candidate lenses to identify potential galaxy-galaxy lenses, investigate multi-colour images available from ground observations of this sub-sample and finally subtract the lens light to verify the lens configuration. Since the first steps in the lens search are based on observation in a single photometric image, this sample offers a perfect

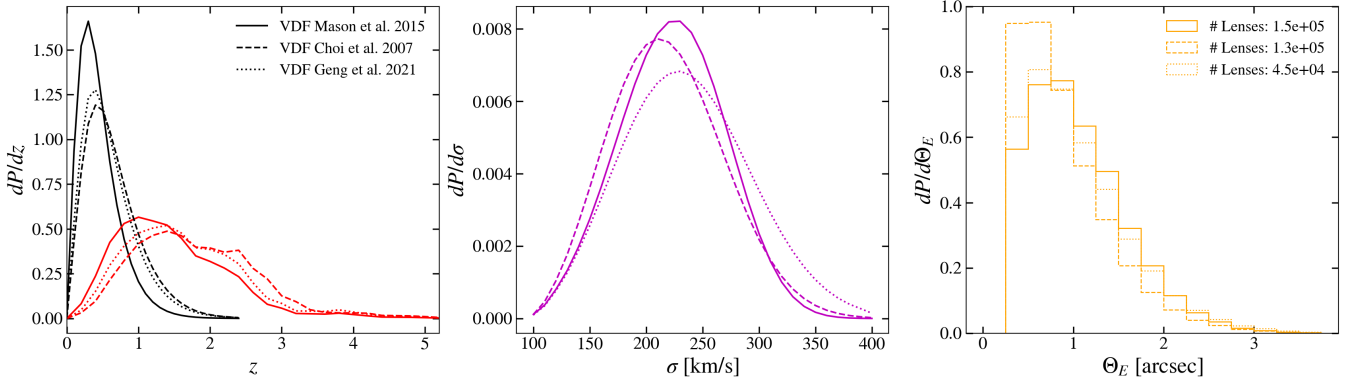


Figure 3. Properties of the lens population as a function of the velocity dispersion function (VDF) profile. The left panel shows the distributions of lens (red) and source (black) redshift for three different VDFs: [Mason et al. 2015](#) (the fiducial distribution assumed in our model, solid line), [Choi et al. 2007](#) (dashed), and [Geng et al. 2021](#) (dotted). The middle panel shows the velocity dispersion distribution. The right panel shows the distribution of Einstein Radii sizes. Here the legend lists the total number of lenses discoverable in Euclid for each VDF considered.

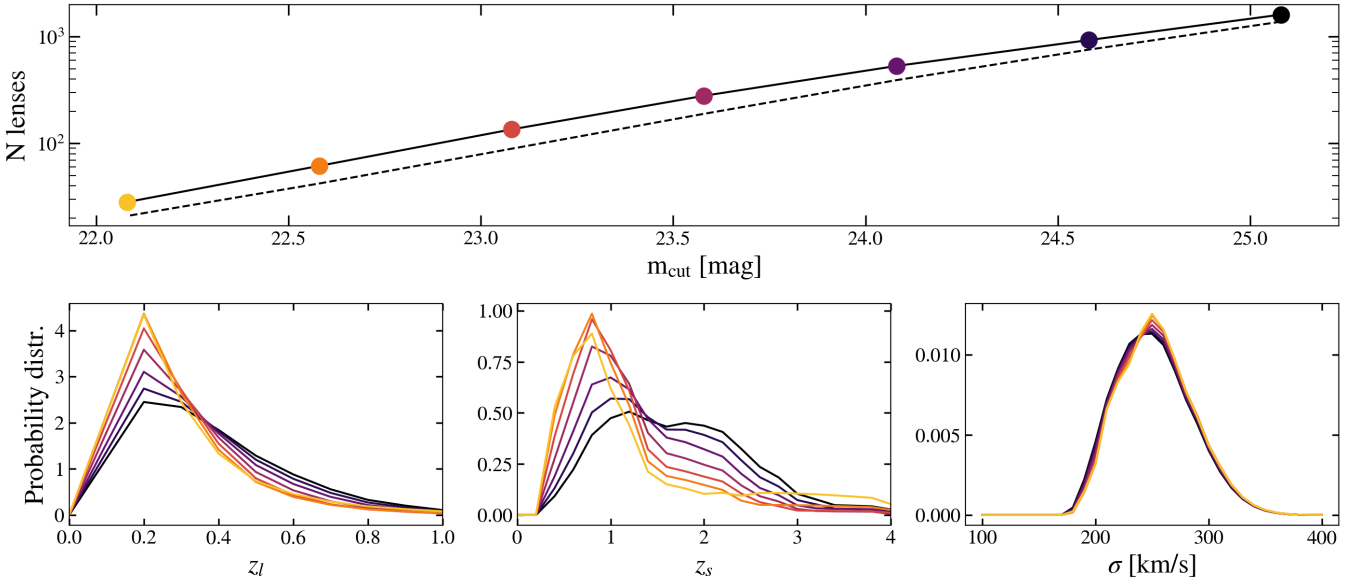


Figure 4. Properties of the lens population as a function of the imposed cut in magnitude. The top panel shows the number of lenses for different choices of m_{cut} (coloured dots) assuming that lens light can be removed (solid line) or with lens light in the sample (dashed line). Following the same colour associated with the value of m_{cut} in the top panel, in the bottom panels are shown the distributions in lens redshift (left), source redshift (middle) and lens velocity dispersion (right).

comparison to test our model predictions. We compare both the full sample of 67 candidate lenses presented in [Faure et al. \(2008\)](#) and the sub-sample with the highest probability (20 lenses). In order to reproduce the limits imposed by the targeted search in [Faure et al. \(2008\)](#), we initialize our model with a restricted range of possible lens redshifts $0.2 < z_l < 1$ and values of velocity dispersion $\sigma > 160$ km/s. We obtain the cut in velocity dispersion from the magnitude cut via the $M_V - \sigma$ relation from [Sahu et al. \(2019\)](#). We use this same $M_V - \sigma$ relation to obtain the distribution of lens magnitudes in the i-band, after accounting for the apparent magnitude accounting for the distance modulus and K-correction. The left panel in [Figure 7](#) shows a good match between the lens redshift distributions of the observed samples and the model, other than a second peak found in the full sample around $z = 1$. This difference might be due to a bias in the visual selection of candidates, or the variance in the photomet-

ric redshift estimation. In the central panel, we see that the model Einstein radii distribution matches that of the full sample well, while the smaller sample of secure lenses is skewed towards larger radii. This might be traced back to the fact that larger Einstein radii make lenses easier to identify by visual inspection and hence be classified as highly probable lenses. Similarly, the apparent magnitude distribution of the lenses in the right panel is skewed towards brighter lenses (i.e., with a larger Einstein radius). Our model predicts 21 (7) lenses, or 13 (4) detectable through the lens light, assuming the VDF from [Mason et al. \(2015\)](#) ([Geng et al. 2021](#)), imposing the lens search observational constraints within the COSMOS HST area. It is important to note that the cosmic variance might play a significant role over a small field: using the COSMIC VARIANCE CALCULATOR from [Trenti & Stiavelli \(2008\)](#) we find that over this field we should expect uncertainty in the number counts of $\approx 24\%$, accounting for the Poisson

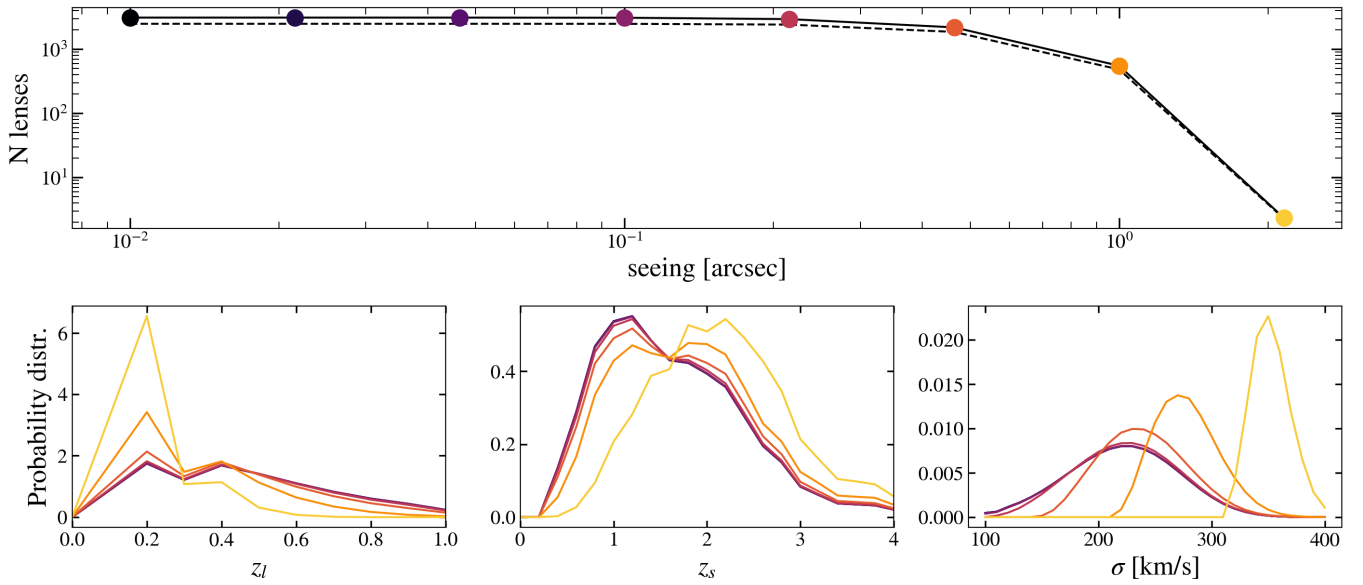


Figure 5. Properties of the lens population as a function of the seeing (or PSF) of the survey. Same panel composition and colour code as in Fig. 4.

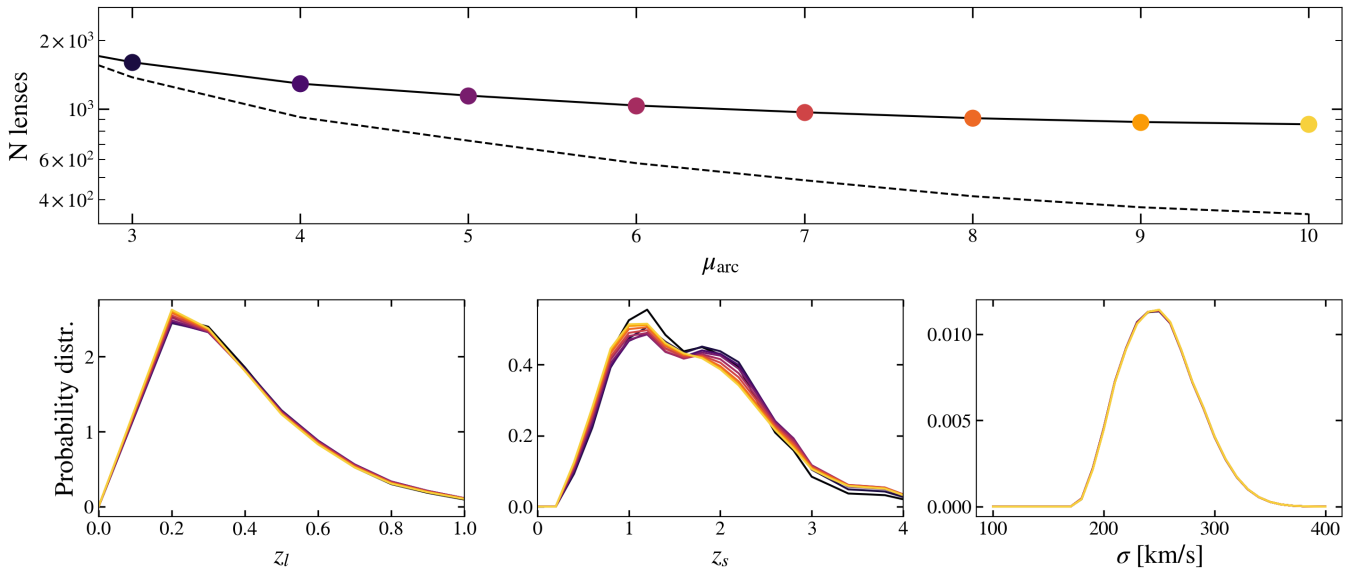


Figure 6. Properties of the lens population as a function of the minimum magnification required for the brightest lensed arc. Same panel composition and colour code as in Fig. 4.

error over 67 galaxies and the cosmic variance of within the pencil beam up to $z_l = 1$ (this becomes $\approx 40\%$ if we consider the sample of 20 high probability candidates). This would make both VDF models compatible with the best sample while favouring a model based on the Mason et al. (2015) VDF if all the candidates in the full sample were genuine lenses.

4.2 Strong Lensing Legacy Survey (SL2S)

The Strong Lensing Legacy Survey (SL2S, Cabanac et al. 2007) was designed to find strong lens systems in the Canada–France–Hawaii Telescope Legacy Survey (CFHTLS). The targeted lens search pro-

cedure in the SL2S is described in Gavazzi et al. (2012) and uses the RINGFINDER algorithm⁵ (Gavazzi et al. 2014), which imposes a limit in magnitude ($i < 22.5$) and redshift ($0.1 < z_l < 0.8$) of the lens, and then looks for blue rings by subtracting a scaled, point-spread function (PSF) matched version of the i -band image from the g -band image. The lens candidates found in the CFHTLS photometry using this algorithm have been followed up with higher-resolution photo-

⁵ This technique is also used in Collett (2015) as one of the two detectability criteria for galaxy scale lenses (the other being the simultaneous satisfaction of multiple images, resolved Einstein ring, pronounced tangential arcs and minimum SNR requirements).

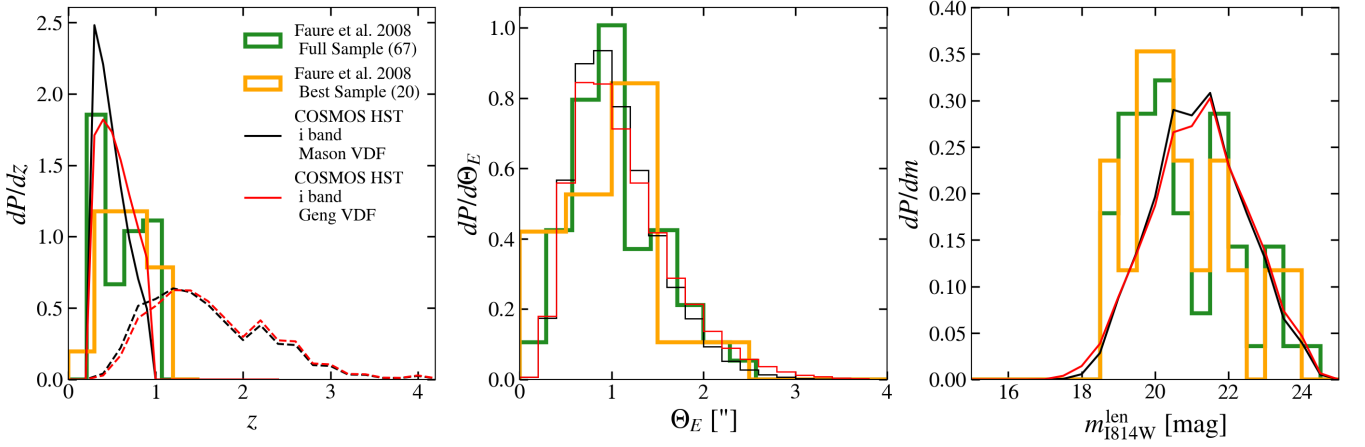


Figure 7. The lens sample statistics from visual inspection on the HST COSMOS data (Faure et al. 2008, full sample in thick green line, best sample in thick orange line) compared to our model expectations for the HST COSMOS i band assuming the VDF from Mason et al. 2015 (in black) or Geng et al. 2021 (in red). The left panel shows the redshift distributions of the lens (solid) and source (dashed) populations. The middle panel shows the distributions of Einstein radii. The right panel shows the distributions of apparent magnitudes of the lens sample. The data bin width is based on the Freedman–Diaconis rule.

metric observations using HST and spectroscopy to determine the redshift and velocity dispersion of the galaxies in the sample. With this setup, Gavazzi et al. (2012) find 2–3 lens candidates per square degree, and Sonnenfeld et al. (2013b) reports 36 secure lenses and 17 lens candidates (for which no spectroscopy was available). We initialize our model with the same restricted range lens redshifts used in the search and velocity dispersion $\sigma > 180$ km/s, obtained from the cut in i -band flux imposed via the K corrected $M_V - \sigma$ relation from Sahu et al. (2019). In Fig. 8 we compare the catalogue of lenses properties in SL2S (Sonnenfeld et al. 2013a, Sonnenfeld et al. 2013b) to the lens statistics predicted by our model for this field, imposing the same constraints on the redshift and velocity dispersion ranges over the CFHTLS Wide field (which observed 171 deg^2 down to $i \approx 24.5$). We compare both the full sample of 53 candidate lenses with available spectroscopic information and the sub-sample of 36 grade A lens candidates. The left panel shows good agreement between the lens redshift distributions of the observed samples and the models, even though the redshift distributions of the background sources appear flatter in the observed distributions, leading to a greater fraction of high redshift sources. The central and right panels show excellent agreement between the velocity dispersion and Einstein radius distributions, respectively. The disagreement of the Einstein radii distribution is consistent with a source redshift distribution skewed towards higher values of z since, for a fixed lens population at centred around $z_l \approx 0.5$, the Einstein radius Θ_E of a source at redshift $z_s \approx 3.5$ would be around 25% larger than Θ_E of a source at redshift $z_s \approx 1.5$. Accounting for the constraints on the lens redshift range from Gavazzi et al. (2012) and the $\approx 25\%$ completeness reached by the RINGFINDER algorithm after visual inspection for magnifications $\mu > 4$ (Gavazzi et al. 2014), our model predicts 174 (51) lenses within the CFHTLS Wide area, or 92 (46) detectable through the lens light, assuming the VDF from Mason et al. (2015) (Geng et al. 2021).

4.3 Machine learning based search in DES

The lens search based on a CNN architecture in Jacobs et al. (2019a) was designed to classify the potential lenses in the DES first data release (Abbott et al. 2018). The training sample for the neural network

was generated from the LENSPOP code described in Collett (2015). The network is trained on a subsample of the lenses that LENSPOP forecasts for DES designed to maximize the difference between the lens and non-lens populations, by tightening the thresholds used for detectability: $\text{SNR}_{\text{min}} = 20$, $\mu_{\text{arc}} = 5$, and an Einstein radius $> 2''$. It is important to note that a neural network trained on a certain volume of the parameter space, could classify objects outside the parameter range it was trained on (e.g., see the redshift range of lenses in Jacobs et al. 2019b). In general, it is therefore impossible to predict how the threshold imposed on the training sample will translate on to the final candidate selection. A follow-up study on the sensitivity of this CNN architecture performance on the degradation of the input parameters (Jacobs et al. 2022) found that the networks are highly sensitive to colour, the simulated PSF used in training, and occlusion of light from a lensed source, but are insensitive to Einstein radius, and performance degrades smoothly with source and lens magnitudes. In Fig. 9 we compare the catalogues of lenses from Jacobs et al. (2019a) and its spectroscopic follow-up, the AGEL survey (Tran et al. 2022), to the lens statistics predicted by our model for the DES field in the i band (which observed $\sim 5000 \text{ deg}^2$ down to $i \approx 23$). The left panel shows that the observed candidate lens distribution is characterized by a higher average redshift compared to our model expectations, is still present in the AGEL survey (see Fig. 7 in Tran et al. 2022). This might suggest that either there is a bias in the lens selection algorithm, or the underlying VDF has to be skewed to higher redshifts. The fact that the apparent magnitudes of the lenses are roughly consistent with our model (right panel), might indicate that the shift in redshift distribution is not due to the VDF profile. The lens search in Jacobs et al. (2019a) yielded 511 lens candidates, while the AGEL sample reports 68 spectroscopically confirmed lenses out of 77 systems selected, giving a successful lens identification rate of $\approx 88\%$. For this field, our model predicts 1822 (440) lenses, or 828 (269) detectable through the lens light, assuming the VDF from Mason et al. (2015) (Geng et al. 2021). Imposing the stricter conditions applied to the training set of the ML model, we expect 479 (139) lenses, or 180 (75) visible through the lens light, using the Mason et al. (2015) (Geng et al. 2021) VDF. On the other hand, assuming that the 88% purity reported in Tran et al. (2022) is constant over the whole ML selected sample, we should expect

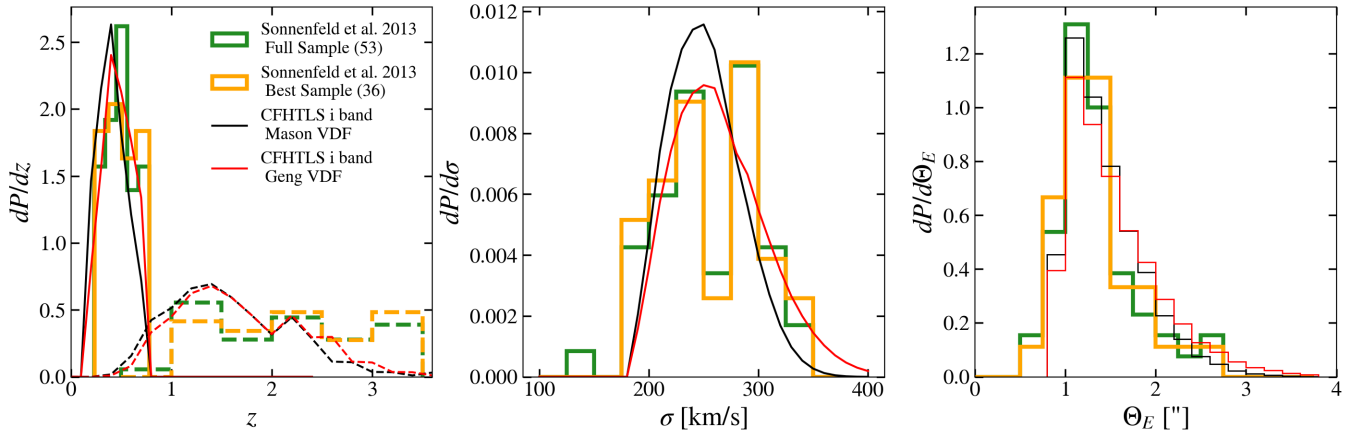


Figure 8. The SL2S lens sample statistics (full sample in thick green line, best sample in thick orange line) compared to our model expectations for the CFHTLS i band assuming the VDF from Mason et al. 2015 (in black) or Geng et al. 2021 (in red). The left panel shows the redshift distributions of the lens (solid) and source (dashed) populations. The middle panel shows the velocity dispersion distributions. The right panel shows the distributions of Einstein radii. The data bin width is based on the Freedman–Diaconis rule.

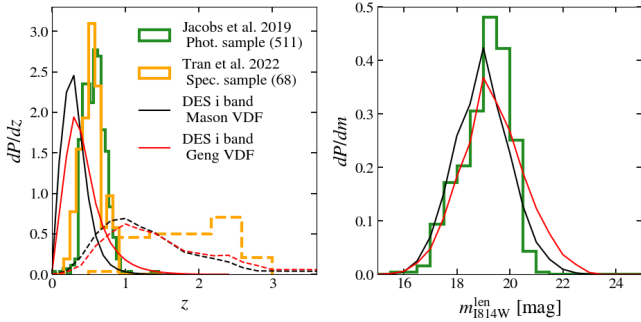


Figure 9. The lens sample statistics from a machine learning based lens search on the DES data (Jacobs et al. 2019a, thick green line) and its spectroscopic follow-up (Tran et al. 2022, thick orange line), compared to our model expectations for the DES i band assuming the VDF from Mason et al. 2015 (in black) or Geng et al. 2021 (in red). The left panel shows the redshift distributions of the lens (solid) and source (dashed) populations. The right panel shows the distributions of apparent magnitudes of the lens sample. The data bin width is based on the Freedman–Diaconis rule.

around 450 lenses in the complete AGEL sample, challenging the VDF redshift evolution in the models considered so far. The choice of the machine learning model and architecture has a strong impact on the proportion of true positives and false positives, which is a measurable quantity in the training and validation process, but could also introduce a bias on the lens and source statistics which is very difficult to quantify. This work could be useful to generate a set of samples drawn from distributions resulting from a range of input parameter values and use these to probe the response of machine learning algorithms.

4.4 SuGOHI

The Survey of Gravitationally-lensed Objects in HSC Imaging (SuGOHI) is an ongoing series of lens searches on the Hyper Suprime-Cam Subaru Strategic Program (HSC SSP, Aihara et al. 2018) survey, based on a variety of different searching techniques. In this section,

we make use of the SuGOHI Candidate List⁶, limiting the analysis to galaxy-galaxy lenses grouped by their grade. The catalogue is constructed combining three lens search methods: feature detection algorithms and model fitting (e.g., YATTALENS in Sonnenfeld et al. 2018, Wong et al. 2018, Wong et al. 2022), human inspection (Jaelani et al. 2020 and Sonnenfeld et al. 2020) and Machine Learning (Jaelani et al. 2023). All of these searches are based on different data releases of the HSC SSP survey, but since they mainly differ in the area covered by the data sample we choose to compare them to the probability distribution based on our model of the final data release of HSC SSP (which observed 1400 deg² down to $i \approx 26.2$). Furthermore, each SuGOHI search features unique selection criteria on the sample of galaxies inspected as lens candidates. In general, all of them restrict the lens search to massive ETGs ($\sigma \gtrsim 230$ km/s) with redshift within $0.2 \lesssim z_l \lesssim 1.0$. After imposing these constraints on our model, we compare it with the properties of the SuGOHI Candidate List as shown in Fig. 10. In the left panel, the observed candidate lens distribution appears more peaked around its central value than our model prediction. This might reflect the prior distribution of luminous red galaxies (LRGs) selected from the Baryon Oscillation Spectroscopic Survey (BOSS) sample as the input sample for the lens search in many of the searches composing the galaxy-galaxy lens catalogue (e.g., see Fig. 7 in Sonnenfeld et al. 2018). The lens magnitude distributions shown in the right panel of Fig. 10 show good agreement between the model and the observations, in particular for the grade B ‘probable’ lenses. Grade A lenses appear to be skewed towards brighter lenses, with larger Einstein radii. For this field, our model predicts $\approx 10^4$ lenses assuming the VDF from Mason et al. (2015), and $\approx 5 \times 10^3$ lenses assuming the Geng et al. 2021 VDF. Since the sample is constructed from different data releases and slightly different pre-selection criteria, we decided to not compare the number of lenses to our models.

4.5 Summary and interpretation of comparisons

In this section, we have compared the results of our model to four lens searches. In all the comparisons we showed the distributions pre-

⁶ <https://www-utap.phys.s.u-tokyo.ac.jp/~oguri/sugohi/>

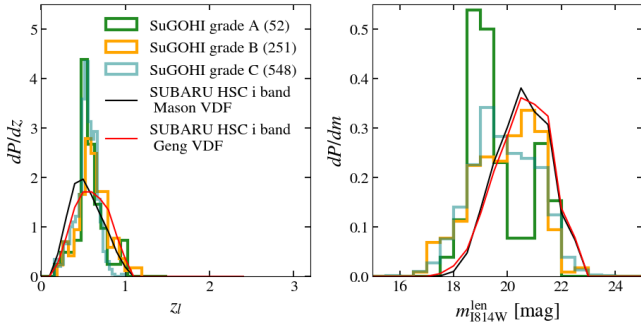


Figure 10. The lens sample statistics from the SuGOHI lens catalogue (Sonnenfeld et al. 2018 and following papers), divided by the lens grade (A in green, B in orange and C in cyan), compared to our model expectations for the DES i band assuming the VDF from Mason et al. 2015 (in black) or Geng et al. 2021 (in red). The left panel shows the redshift distributions of the lens (solid) and source (dashed) populations. The right panel shows the distributions of apparent magnitudes of the lens sample. The data bin width is based on the Freedman–Diaconis rule.

dicted by our model for two different choices of VDF, after applying the constraints on the parameter space (e.g., redshift, magnitude, or Einstein radius of the lens) adopted in each lens search. The results of these models are listed in Table 3.

Our model shows good agreement between the lens apparent magnitude (obtained from the lens velocity dispersion) and Einstein radii distribution across all surveys. The predicted lens and source redshift distributions match well with the results of the COSMOS HST and SL2S surveys, but show some tension with the redshift distributions in SuGOHI and the outcomes of the ML-based search on DES data. These differences might be traced back to the difference in the completeness of the search methods over the range of redshift considered, even though further work is needed to constrain the VDF evolution with cosmic time and rule out the possibility of observed redshift distributions being linked to the lens population. The number of lenses predicted by our model agrees with the observed number counts in Faure et al. (2008) and Tran et al. (2022), after imposing the constraints on z_l , σ , z_s , and Θ_E of the related lens search method. This agreement provides additional validation of our model. In fact, Faure et al. (2008) find 20 probable lenses in COSMOS HST, and our model predicts between 4 and 21 identifiable lenses in the same field, depending on the assumed VDF and the ability to remove the lens light. Similarly, given the purity of the Tran et al. (2022) we can expect around 450 lenses in DES, which is within our predicted range of 75 to 479 lenses that can be found within the constraints of their search method. Using the same parameter range of the lens population as imposed in Sonnenfeld et al. (2013a), we predict a total of 46 to 174 lenses in the CFHTLS. Since the SuGOHI Candidate List is constructed using different data releases (i.e., sky areas) and different search methods, we do not compare its number of lenses to our predictions.

The comparison with past lens searches conducted in this Section shows that our model gives a reliable estimate of the number and distribution of identifiable lenses in surveys. We therefore turn to predictions for future surveys in the following section.

5 FORECAST OF STRONG LENS YIELDS IN SURVEYS

In this section we investigate the galaxy scale lens and source populations in a range of ground-based and space-based surveys, encompassing a range of areas, depth and photometric bands, as listed in Table 4. We forecast the expected number of lenses assuming that the lens light can (not) be completely removed, which gives us an upper (lower) limit on the lens yield of a given survey. We also compute the lens statistics for each survey using two different choices of VDF (Mason et al. 2015 and Geng et al. 2021). We then compare the distributions of three surveys (EUCLID Wide, LLST, DES) and the JWST PEARLS NEP field in Fig. 11.

As expected, the photometric band in which we conduct the observations impacts the number of detectable lenses and the fraction of high-redshift sources, although this is mostly due to the change in survey depth between bands. For example sources with redshift $z_s < 5.3$ can be detected in the i -band, while sources up to $z_s \lesssim 12$ can be seen in the F150W band. However, in the case of photometric surveys, the upper bound on the maximum redshift detectable usually comes from the combination of the survey magnitude limit and the luminosity density of the source population. This is why in Fig. 11 the redshift distribution of the JWST PEARLS NEP field, which is extremely deep, is skewed to higher values of both lens and source redshift compared to the distributions of the other surveys shown in the same panel. On the other hand, the final co-added sample of lenses from LSST is expected to have a lower central value for the lens redshift distribution and a comparatively high average source redshift. This is not due to the band or flux limit, but rather to the limit on the smallest Einstein ring that can be resolved. In fact, for an isothermal lens, the Einstein radius is proportional to the ratio of angular diameter distances D_{ls}/D_s , and hence surveys with large seeing/PSF (e.g., ground-based imaging) can not probe high redshift and low mass deflectors, as they have smaller Einstein radii (for fixed source redshift). For example, in Fig. 11 we can see how the distributions of Einstein radii in DES are characterized by a larger lower bound compared to LSST observed in the same band. This drives DES to have a lens redshift distribution peaked around a smaller value of z_l and a lens velocity dispersion distribution centred around a higher value of σ compared to the lens population observable by LSST.

This shows that the properties of ETGs that are most likely to be a lens depend on the characteristics of the telescope and survey. Hence lens-based searches (i.e., searches that look for lenses around a pre-selected sample of ETGs), should choose the selection criteria for the potential lens population after simulating the expected distributions in parameter space to minimize the loss of identifiable lenses.

We find that Euclid, Roman and Vera Rubin telescope wide surveys will yield $O(10^5)$ lenses, with the exact number varying by up to a factor of 4 depending on the ability to remove the lens light and the lens mass distribution (or VDF). The predicted surface density of lenses identifiable through the lens light (indicated in Table 4) shows a wide range of expected values. For example, the Euclid Wide survey and a single visit of LSST should expect a few lenses per square degree, while a deep JWST field should expect around 50 to 100 lenses per square degree. More details for some combinations of surveys and observing photometric bands can be found in Table 4.

The comparisons conducted in the previous section might suggest that the actual number of identifiable lenses can be significantly smaller, depending on the search method and specific constraints applied to the observed data.

Table 3. Galaxy-galaxy lensing yields an estimate for a selection of past lens searches.

Telescope	Survey	Filter	Seeing (PSF) ["]	Area [deg ²]	Exp. time [sec]	m_{cut} [mag]	m_{lim} [mag]	N VDF M	N VDF G	N [deg ⁻²]	Ref.
(1)	(2)	(3)	(4)	(5)	(6)	(7)	(8)	(9)	(10)	(11)	(12)
HST	COSMOS	F814W	0.120	1.60	2000	25.0	26.5	36 (17)	11 (7)	10 4	1
	COSMOS (F)							21 (13)	7 (4)	8 2	
CHFT	CHFTLS	i	0.620	170	5500	24.5	25.1	975 (525)	268 (185)	3 1	2
	CHFTLS (S)							174 (92)	51 (46)	0.54 0.27	
DECam	DES	i	0.960	5000	900	23.0	24.7	1822 (828)	440 (269)	0.17 0.05	3
	DES (J)							479 (180)	139 (75)	0.04 0.02	
HSC	HSC-SSP	i	0.600	1400	8000	26.2	26.2	$5.2 (2.8) \times 10^4$	$1.6 (1.2) \times 10^4$	20 9	4
	HSC-SSP (Su)							$2.3 (1.7) \times 10^4$	$0.9 (0.7) \times 10^4$	12 5	

Notes. The columns indicate the (1) telescope, (2) survey, and (3) photometric filter considered. (4) The seeing (or PSF for space-based telescopes) in arcseconds. (5) The area of a survey in square degrees. (6) The exposure time in seconds. (7) The magnitude cut and (8) the limit magnitude. (9 - 10) The total number of identifiable lenses, with lens light (not) removed, assuming the VDF described in [Mason et al. 2015](#) and [Geng et al. 2021](#), respectively. (11) The surface number density, in square arcseconds, of the lenses identifiable through the foreground lens light, assuming the VDF described in [Mason et al. 2015](#) and [Geng et al. 2021](#), respectively. (12) The references for the input parameters. When an initial is indicated in parenthesis, as in (F), it indicates a set of additional constraints on the lens and/or source distribution imposed by a particular lens search. The (F) refers to the lens search in the COSMOS field by [Faure et al. 2008](#), (S) to the lens search in the CHFTLS field by [Sonnenfeld et al. 2013a](#), (J) to the lens search in the DES field by [Jacobs et al. 2019b](#), and (Su) to the lens search in the HSC-SSP field by [Sonnenfeld et al. 2018](#) and following SuGOHI papers.

Ref. ¹ [Scoville et al. 2007](#), ² [Cabanac et al. 2007](#), ³ [Abbott et al. 2018](#), ⁴ [Aihara et al. 2018](#).

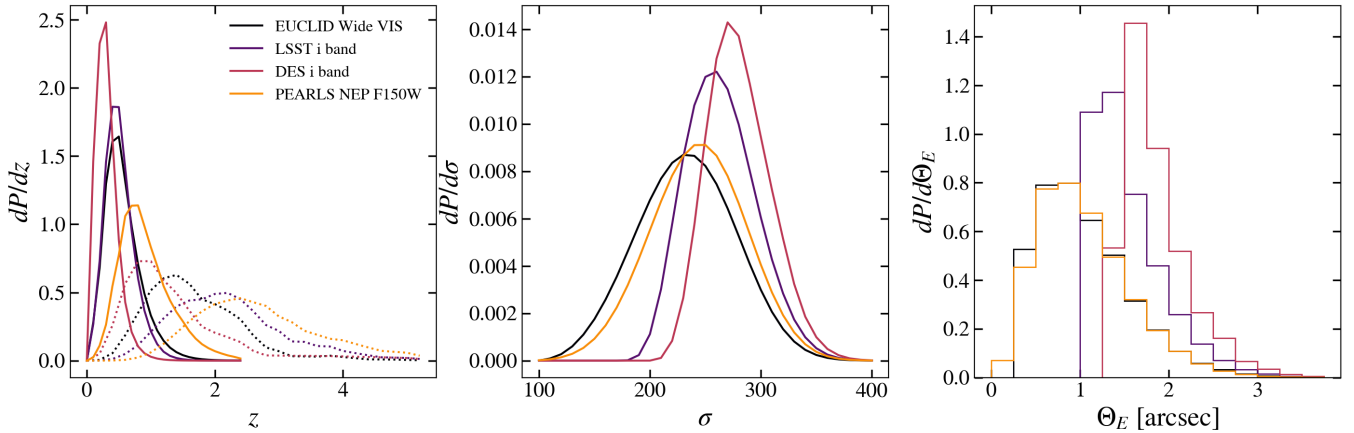


Figure 11. Properties of the forecasted lens samples in a selection of wide and narrow field surveys, adopting the [Mason et al. 2015](#) VDF. The left panel shows the redshift distributions of the lens (solid) and source (dotted) populations. The middle and right panels show the velocity dispersion and the Einstein radius distributions, respectively. Black shows Euclid, purple shows Vera Rubin LSST, red shows DES and orange shows the JWST PEARLS NEP field.

6 RARE LENSES

The large samples of strong lenses that will be discovered with upcoming wide area surveys will contain rare configurations such as double plane systems and quad lenses.

6.1 Dual lenses

A single galaxy might act as a lens for more than one background source, in general at different redshifts (excluding two merging galaxies as the source). This multiple lens plane configuration might be used as a cosmography tool to probe global cosmological parameters such as Ω_m or Ω_Λ , via the ratio of cosmological distances entering the lensing potential (e.g. [Gavazzi et al. 2008](#)).

An order of magnitude estimate of the probability of observing multiple sources behind a single lens can be obtained by applying Poisson statistics to the *a-priori* probability $\tau(z_s)$ of lensing a source at redshift z_s . Defining $P(N)$ as the probability of detecting a lens

with N source planes, we should expect around $P(2)/P(1) = \tau/2!$ double lenses per single lens, or one in $\sim 10^3$.

For a more thorough calculation, assuming the lensing cross sections of the two populations of sources are independent ([Gavazzi et al. 2008](#)), we can write the number of double lenses as

$$N_{s1,s2} = \int dz_{s2} \int dz_{s1} \int dM_{s2} \int dM_{s1} \int dz_l \int d\sigma \Phi(\sigma, z_l) \times \frac{dN_{SL}^{obs}(M_{s1}, z_{s1} | \sigma, z_l)}{dz_{s1} dM_{s1}} \frac{dN_{SL}^{obs}(M_{s2}, z_{s2} | \sigma, z_l)}{dz_{s2} dM_{s2}} \frac{dV(A_s, z_l)}{dz_l}. \quad (16)$$

Applying Eq. 16 to Euclid Wide VIS, we predict 154 (28) double lenses, assuming lens light can (not) be removed (see Fig. 12). This implies a fraction of double lenses of 1×10^{-3} (0.3×10^{-3}). Increasing the depth of the survey yields a higher fraction of double lenses, up to a fraction of $\sim 3 \times 10^{-3}$. A ratio of a double lens every thousand lenses is compatible with observations, given that so far have found

Table 4. Galaxy-galaxy lensing yields estimate for a selection of ongoing and future surveys observing in the visible/NIR.

Telescope	Survey	Filter	Seeing (PSF) ["]	Area [deg ²]	Exp. time [sec]	m_{cut} [mag]	m_{lim} [mag]	N VDF M	N VDF G	N [deg ⁻²]	Ref.
JWST	COSMOS Web	F115W	0.040	0.54	516	26.13	27.13	46 (15)	16 (8)	28 15	1
		F150W	0.050	0.54	516	26.35	27.35	74 (14)	25 (8)	26 15	
		F277W	0.092	0.54	516	27.00	27.99	121 (15)	42 (10)	28 19	
	PEARLS NEP	F115W	0.040	0.015	11680	27.76	28.76	4 (1)	1 (1)	57 31	2
		F150W	0.050	0.015	11680	27.91	28.91	8 (1)	3 (1)	73 46	
		F277W	0.092	0.015	11680	27.81	28.81	7 (1)	3 (1)	43 31	
Euclid	Wide	VIS	0.170	15000	2280	24.50	24.50	$1.5 (0.9) \times 10^5$	$4.5 (3.2) \times 10^4$	6 2	3
		Y	0.220	15000	448	24.00	24.00	$0.5 (0.2) \times 10^5$	$1.3 (0.7) \times 10^4$	1 1	
		J	0.300	15000	448	24.00	24.00	$0.8 (0.4) \times 10^5$	$2.4 (1.4) \times 10^4$	2 1	
		H	0.360	15000	448	24.00	24.00	$1.2 (0.4) \times 10^5$	$3.3 (1.5) \times 10^4$	2 1	
Roman	High Latitude Wide-Area	J129	0.300	1700	146	26.7	26.7	$4.5 (1.7) \times 10^4$	$1.4 (0.8) \times 10^4$	10 5	4
Vera Rubin (LSST)	single visit	i	0.710	20000	30	23.41	23.41	$2.2 (1.3) \times 10^4$	$5.7 (4.2) \times 10^3$	1 0.24	5
	final co-added	i	0.710	20000	6000	26.40	26.40	$7.4 (3.8) \times 10^5$	$2.4 (1.7) \times 10^5$	19 8	

Notes. This Table follows the same structure as Table 3.

Ref. ¹ Casey et al. 2023, ² Windhorst et al. 2023, ³ Euclid Collaboration et al. 2022, ⁴ Spergel et al. 2015, ⁵ Ivezić et al. 2019.

only a handful of double lenses (Gavazzi et al. 2008, Tu et al. 2009, Tanaka et al. 2016, Schuldt et al. 2019) out of the $\sim 10^3$ discovered lenses.

6.2 Quads

Adopting the formalism developed in Section 2.3, we find that $\sim 4\%$ of the lenses should be in a quad configuration, which is lower than previous estimates on galaxy-quasar lenses (e.g., $\sim 10\%$ in Oguri & Marshall 2010, and 9% Sonnenfeld et al. 2023). However, our value is consistent with existing observations of galaxy-galaxy (e.g., 5% in More et al. 2016). The differences between these estimates are due to the different choices in the lens mass distribution and its evolution with redshift, in the distribution of axis ratio in lenses, and in the luminosity density of sources compared to the survey limit. The estimate of Oguri & Marshall (2010) is based on a SIE lens with an external shear component, and normally distributed ellipticities centred on an axis ratio of $f = 0.7$. Sonnenfeld et al. 2023 finds a quad fraction of 9% , using a composite lens model (projected Sérsic profile for the stellar component and a projected NFW profile for the dark matter component) and an axis ratio distribution set to a beta distribution with $\alpha = 6.28$ and $\beta = 2.05$. Quads are biased towards more elliptical lenses (Sonnenfeld et al. 2023), because the size in the source plane of the inner caustic increases with decreasing axis ratio f , and larger-sized sources, as they are more likely to overlap with the inner caustic. For this reason, the exact value of this fraction comes directly from our assumption about the ellipticity distribution of the lens population. On the other hand, this implies that quads can be used as probes of ellipticity. The mass distribution of the lens population becomes important when considering extended sources. We discuss the overall effect of proper modelling of extended sources lensing in the following Section.

7 DISCUSSION

This paper has presented an analytic model for lens statistics which adopts a set of prescriptions motivated by observational and theoretical constraints on the deflector and source populations. In this section

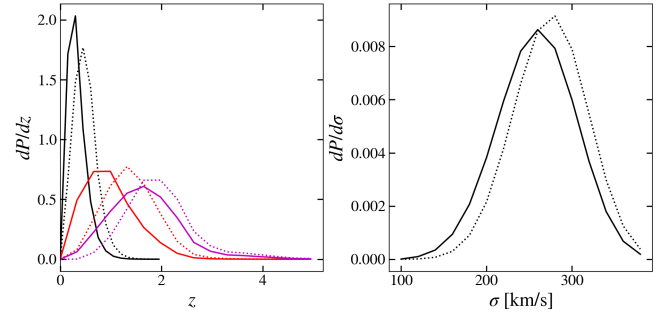


Figure 12. Lens and sources redshift (left) and velocity dispersion (right) distributions for the population of detectable dual plane lenses. In the left panel, the lens redshift is shown in black, the first source redshift is red, and the second source redshift is magenta. The solid (dotted) line represents the lenses detectable when the source light is (not) removed.

we discuss the approximations we used to construct our model, focusing on the regimes where these simplifying assumptions are sufficient to describe the lens statistics and the cases where these assumptions should be refined.

7.1 Improving the lens model

We have assumed that the lens population is composed of early-type galaxies with an isothermal total mass profile. While this assumption is well suited to describe the overall properties of a sample of galaxy scale lenses, different choices of lens mass profiles could affect both the lensing cross-section and the magnification probability distribution.

One potential improvement is to sample the deflector population from a simulation rather than model it analytically. While this gives a much higher level of detail on the projected mass and light distribution of a lens compared to an analytical approximation, it is often limited to a maximum stellar mass given by the simulation volume (e.g., $< 10^{11.5} M_{\odot}$ in Holloway et al. 2023b). This might lead to biases in the lens statistics, especially when compared to lens searches targeted around bright ETGs (e.g. Fig. 7 in Sonnenfeld et al. 2018).

For example, using the M_* - σ relation from [Cannarozzo et al. \(2020\)](#) to map the upper bound in stellar mass to a cut in the VDF, we find that lensing estimators based on realizations of galaxy catalogues might underestimate the amount of low redshift ($0 < z \lesssim 0.5$) gal-gal lenses a factor of ~ 2 , especially in deep surveys.

Furthermore, analytical estimates for the lensing cross section as a function of source size and flux, as well as the dark matter fraction and slope for a lens with a generalized Navarro-Frenk-White mass component ([Wyithe et al. 2001](#)), have been studied in [Sonnenfeld et al. \(2023\)](#) and could be integrated into our current model.

Another improvement would be to include external shear, which can boost the magnification of background sources. A full characterization of the line-of-sight environment is beyond the scope of this paper, but [Collett \(2015\)](#) showed that a simple estimate using normally distributed shear components with values compatible to existing models of gal-gal lenses gives a $\sim 5\%$ boost in the number of lens systems. The total number of lenses predicted by the model is not very sensitive to small changes in the ellipticity distribution of the deflector population, in agreement with [Collett \(2015\)](#), while the number of quad configuration lenses is strongly correlated with the flattening of the lenses.

7.2 Improving the source model

Our model does not explicitly account for the differential magnification of extended sources. Since extended sources are subject to an overall lower magnification, this motivates movement away from analytical models, in favour of simulation-based analyses ([Collett 2015](#)). However, we argue that the inclusion of extended sources has a small effect on the summary statistics of lensing models, although it could be important when considering a sub-sample of highly-magnified sources. Figure 2 of [Ferrami & Wyithe \(2023\)](#) shows that the magnification bias for extended sources is the same as for point-like sources in the power-law regime of the luminosity function. Hence, our model will be impacted only for sources in the very bright end of the luminosity function, which contribute a negligible fraction of the total number of detectable galaxies (Eqs. 7 - 9). Extended sources should also increase our expected fraction of quad configurations, as they would be more likely to overlap with the inner caustic. Moreover, studying the ratio between the area of the inner caustic and the sizes of the source population would be important for study of the statistics of complete Einstein rings.

We can get an upper bound on the effect of extended sources by looking at the integral of the SIE magnification distribution up to a maximum magnification (that depends on the source size). Approximating sources as circles with uniform luminosity, a galaxy with an angular radius of half the Einstein radius can attain a maximum magnification of $\mu_{\max} \approx 4$ (see Fig. 1 in [Ferrami & Wyithe 2023](#)). We calculate the fraction of lenses with brightest image having $\mu < \mu_{\max}$ as $\int_2^4 d\mu \frac{dP}{d\mu} = \int_2^4 d\mu \frac{2}{(\mu-1)^3} = 8/9$. This indicates that a population of extremely large sources would at most have a difference in the expected number of lenses of $\approx 12\%$ (since most of the source population lies in the faint end of the luminosity function)⁷. In the future, we plan to extend this model to handle extended sources.

⁷ Furthermore, the size-maximum magnitude relation evolves quite rapidly. A source with a size of 10% the Einstein Radius of the lens has a maximum magnification of $\mu_{\max} \approx 10$, which leads to a difference of 80/81, or less than 2% difference with a point source population.

7.3 Improving flux limits

In future work, we plan to explore alternative thresholds for lens detection other than minimum magnification. While imposing a minimum magnification is a useful approach from a modelling-based perspective, it is non-trivial to determine the distribution of magnifications of a lens sample from observations. This is in part due to the mass-sheet degeneracy ([Falco et al. 1985](#)).

8 CONCLUSIONS

In this paper, we have presented a flexible model for computing the expected population of detectable lenses in photometric surveys. We tested our model on four samples of lenses from past searches, COSMOS HST, SL2S, SuGOHI, and a lens search in the DES data.

The number of lenses, lens redshift, magnitude, and Einstein radii distributions predicted by our model provide a good match against the lens samples from COSMOS HST and SL2S where completeness and selection can be modelled, and for Einstein radii distributions in all samples. On the other hand, such differences might also indicate that the properties of the lens population are not well represented by the Velocity Dispersion Functions considered in this paper, and further work will be needed to properly address these tensions. We then computed the expected number of lenses in several ongoing and future surveys, including Euclid Wide, Vera Rubin Observatory LSST, and the Roman Space Telescope High Latitude Wide Area, along with the forecast lens searches in deeper and smaller areas using JWST photometry. We found that the assumed velocity dispersion function and the cut in magnitude have the greatest impact on the detectable lens and source populations. Our model predicts a yield of $\mathcal{O}(10^5)$ lenses from future wide-area surveys, in agreement with previous estimates. We estimated the number of double plane lenses in Euclid (around 150), or around 0.1%, consistent with the available observations. This expected increase of two orders of magnitude of the available sample of double lenses will greatly increase their statistical power for cosmography. Our model predicts a fraction of quad lenses around 4%, also consistent with available samples of galaxy-galaxy lenses.

The code used in this work is made publicly available⁸.

ACKNOWLEDGMENTS

We wish to thank K. Wong, J. Cuby, M. Oguri, Y. Harikane, K. Glazebrook, and C. Jacobs for useful discussions that improved the scope of this work. This research was supported by the Australian Research Council Centre of Excellence for All Sky Astrophysics in 3 Dimensions (ASTRO 3D), through project number CE170100013.

DATA AVAILABILITY

The code and the modelled data discussed in this paper are publicly available at <https://github.com/Ferr013/GALESS>.

⁸ The code is available at <https://github.com/Ferr013/GALESS>

REFERENCES

- Abbott T. M. C., et al., 2018, *ApJS*, 239, 18
- Aihara H., et al., 2018, *PASJ*, 70, S4
- Alard C., 2006, *arXiv e-prints*, pp astro-ph/0606757
- Angora G., et al., 2023, *A&A*, 676, A40
- Barone-Nugent R. L., Wyithe J. S. B., Trenti M., Treu T., Oesch P., Bouwens R., Illingworth G. D., Schmidt K. B., 2015, *MNRAS*, 450, 1224
- Birrer S., et al., 2020, *A&A*, 643, A165
- Blandford R. D., Narayan R., 1992, *ARA&A*, 30, 311
- Bouwens R. J., et al., 2014, *ApJ*, 793, 115
- Bouwens R. J., Illingworth G., Ellis R. S., Oesch P., Stefanon M., 2022, *ApJ*, 940, 55
- Cabanac R. A., et al., 2007, *A&A*, 461, 813
- Cannarozzo C., Sonnenfeld A., Nipoti C., 2020, *MNRAS*, 498, 1101
- Casey C. M., et al., 2023, *ApJ*, 954, 31
- Chan J. H. H., Suyu S. H., Chiueh T., More A., Marshall P. J., Coupon J., Oguri M., Price P., 2015, *ApJ*, 807, 138
- Choi Y.-Y., Park C., Vogeley M. S., 2007, *ApJ*, 658, 884
- Collett T. E., 2015, *ApJ*, 811, 20
- Collett T. E., Auger M. W., 2014, *MNRAS*, 443, 969
- Collett T. E., et al., 2018, *Science*, 360, 1342
- Collett T. E., et al., 2023, *The Messenger*, 190, 49
- Despali G., Vegetti S., White S. D. M., Giocoli C., van den Bosch F. C., 2018, *MNRAS*, 475, 5424
- Diehl H. T., et al., 2017, *ApJS*, 232, 15
- Djorgovski S., Davis M., 1987, *ApJ*, 313, 59
- Dressler A., Lynden-Bell D., Burstein D., Davies R. L., Faber S. M., Terlevich R., Wegner G., 1987, *ApJ*, 313, 42
- Etherington A., et al., 2022, *MNRAS*, 517, 3275
- Etherington A., et al., 2023, *MNRAS*, 521, 6005
- Euclid Collaboration et al., 2022, *A&A*, 662, A112
- Euclid Collaboration et al., 2023, *arXiv e-prints*, p. arXiv:2307.08736
- Falco E. E., Gorenstein M. V., Shapiro I. I., 1985, *ApJ*, 289, L1
- Faure C., et al., 2008, *ApJS*, 176, 19
- Ferrami G., Wyithe J. S. B., 2023, *MNRAS*, 523, L21
- Gavazzi R., Treu T., Rhodes J. D., Koopmans L. V. E., Bolton A. S., Burles S., Massey R. J., Moustakas L. A., 2007, *ApJ*, 667, 176
- Gavazzi R., Treu T., Koopmans L. V. E., Bolton A. S., Moustakas L. A., Burles S., Marshall P. J., 2008, *ApJ*, 677, 1046
- Gavazzi R., Treu T., Marshall P. J., Braut F., Ruff A., 2012, *ApJ*, 761, 170
- Gavazzi R., Marshall P. J., Treu T., Sonnenfeld A., 2014, *ApJ*, 785, 144
- Geng S., Cao S., Liu Y., Liu T., Biesiada M., Lian Y., 2021, *MNRAS*, 503, 1319
- Grillo C., 2010, *ApJ*, 722, 779
- Grillo C., Lombardi M., Bertin G., 2008, *A&A*, 477, 397
- Grillo C., Gobat R., Lombardi M., Rosati P., 2009, *A&A*, 501, 461
- Hartley P., Flamary R., Jackson N., Tagore A. S., Metcalf R. B., 2017, *MNRAS*, 471, 3378
- He Z., et al., 2020, *MNRAS*, 497, 556
- Hogg D. W., Blandford R., Kundic T., Fassnacht C. D., Malhotra S., 1996, *ApJ*, 467, L73
- Holloway P., Marshall P. J., Verma A., More A., Cañameras R., Jaelani A. T., Ishida Y., Wong K. C., 2023a, *arXiv e-prints*, p. arXiv:2311.07455
- Holloway P., Verma A., Marshall P. J., More A., Tecza M., 2023b, *MNRAS*, 525, 2341
- Ivezic Z., et al., 2008, *Serbian Astronomical Journal*, 176, 1
- Ivezic Z., et al., 2019, *ApJ*, 873, 111
- Jacobs C., Glazebrook K., Collett T., More A., McCarthy C., 2017, *MNRAS*, 471, 167
- Jacobs C., et al., 2019a, *ApJS*, 243, 17
- Jacobs C., et al., 2019b, *MNRAS*, 484, 5330
- Jacobs C., Glazebrook K., Qin A. K., Collett T., 2022, *Astronomy and Computing*, 38, 100535
- Jaelani A. T., et al., 2020, *MNRAS*, 495, 1291
- Jaelani A. T., More A., Wong K. C., Inoue K. T., Chao D. C. Y., Premadi P. W., Cañameras R., 2023, *arXiv e-prints*, p. arXiv:2312.07333
- Joseph R., et al., 2014, *A&A*, 566, A63
- Kochanek C. S., 1996, *ApJ*, 466, 638
- Koopmans L. V. E., Treu T., 2003, *ApJ*, 583, 606
- Koopmans L. V. E., et al., 2009, *ApJ*, 703, L51
- Kormann R., Schneider P., Bartelmann M., 1994, *A&A*, 284, 285
- La Barbera F., de Carvalho R. R., de La Rosa I. G., Lopes P. A. A., Kohl-Moreira J. L., Capelato H. V., 2010a, *MNRAS*, 408, 1313
- La Barbera F., de Carvalho R. R., de La Rosa I. G., Lopes P. A. A., 2010b, *MNRAS*, 408, 1335
- Lapi A., Negrello M., González-Nuevo J., Cai Z. Y., De Zotti G., Danese L., 2012, *ApJ*, 755, 46
- Liu C., Mutch S. J., Angel P. W., Duffy A. R., Geil P. M., Poole G. B., Mesinger A., Wyithe J. S. B., 2016, *MNRAS*, 462, 235
- Mao S., Schneider P., 1998, *MNRAS*, 295, 587
- Marshall P., Blandford R., Sako M., 2005, *New Astron. Rev.*, 49, 387
- Marshall P. J., Hogg D. W., Moustakas L. A., Fassnacht C. D., Bradač M., Schrabback T., Blandford R. D., 2009, *ApJ*, 694, 924
- Marshall P. J., et al., 2016, *MNRAS*, 455, 1171
- Mason C. A., et al., 2015, *ApJ*, 805, 79
- Mondal C., Saha K., Windhorst R. A., Jansen R. A., 2023, *ApJ*, 946, 90
- More A., Cabanac R., More S., Alard C., Limousin M., Kneib J. P., Gavazzi R., Motta V., 2012, *ApJ*, 749, 38
- More A., et al., 2016, *MNRAS*, 455, 1191
- Moustakas L. A., et al., 2007, *ApJ*, 660, L31
- Nightingale J. W., Dye S., 2015, *MNRAS*, 452, 2940
- O'Donnell J. H., et al., 2022, *ApJS*, 259, 27
- Oguri M., Marshall P. J., 2010, *MNRAS*, 405, 2579
- Oguri M., et al., 2012, *AJ*, 143, 120
- Oldham L. J., Auger M. W., 2018, *MNRAS*, 476, 133
- Pawase R. S., Courbin F., Faure C., Kokotanekova R., Meylan G., 2014, *MNRAS*, 439, 3392
- Pei Y. C., 1995, *ApJ*, 440, 485
- Refsdal S., 1964, *MNRAS*, 128, 307
- Sahu N., Graham A. W., Davis B. L., 2019, *ApJ*, 887, 10
- Schuldts S., Chirivì G., Suyu S. H., Yıldırım A., Sonnenfeld A., Halkola A., Lewis G. F., 2019, *A&A*, 631, A40
- Schwab J., Bolton A. S., Rappaport S. A., 2010, *ApJ*, 708, 750
- Scoville N., et al., 2007, *ApJS*, 172, 38
- Serjeant S., 2014, *ApJ*, 793, L10
- Shajib A. J., Treu T., Birrer S., Sonnenfeld A., 2021, *MNRAS*, 503, 2380
- Shajib A. J., et al., 2023, *A&A*, 673, A9
- Shibuya T., Ouchi M., Harikane Y., 2015, *ApJS*, 219, 15
- Smith R. J., Lucey J. R., Conroy C., 2015, *MNRAS*, 449, 3441
- Sonnenfeld A., 2022a, *A&A*, 659, A132
- Sonnenfeld A., 2022b, *A&A*, 659, A133
- Sonnenfeld A., Cautun M., 2021, *A&A*, 651, A18
- Sonnenfeld A., Gavazzi R., Suyu S. H., Treu T., Marshall P. J., 2013a, *ApJ*, 777, 97
- Sonnenfeld A., Treu T., Gavazzi R., Suyu S. H., Marshall P. J., Auger M. W., Nipoti C., 2013b, *ApJ*, 777, 98
- Sonnenfeld A., Treu T., Marshall P. J., Suyu S. H., Gavazzi R., Auger M. W., Nipoti C., 2015, *ApJ*, 800, 94
- Sonnenfeld A., et al., 2018, *PASJ*, 70, S29
- Sonnenfeld A., Jaelani A. T., Chan J., More A., Suyu S. H., Wong K. C., Oguri M., Lee C.-H., 2019, *A&A*, 630, A71
- Sonnenfeld A., et al., 2020, *A&A*, 642, A148
- Sonnenfeld A., Li S.-S., Despali G., Gavazzi R., Shajib A. J., Taylor E. N., 2023, *A&A*, 678, A4
- Spergel D., et al., 2015, *arXiv e-prints*, p. arXiv:1503.03757
- Stein G., Blaum J., Harrington P., Medan T., Lukić Z., 2022, *ApJ*, 932, 107
- Stockmann M., et al., 2021, *The Astrophysical Journal*, 908, 135
- Suyu S. H., et al., 2017, *MNRAS*, 468, 2590
- Tan C. Y., et al., 2023, *arXiv e-prints*, p. arXiv:2311.09307
- Tanaka M., et al., 2016, *ApJ*, 826, L19
- Thuruthipilly H., Zdrozny A., Pollo A., Biesiada M., 2022, *A&A*, 664, A4
- Tran K.-V. H., et al., 2022, *AJ*, 164, 148
- Trenti M., Stiavelli M., 2008, *ApJ*, 676, 767
- Treu T., 2010, *ARA&A*, 48, 87
- Treu T., Koopmans L. V. E., 2002, *ApJ*, 575, 87

- Treu T., Stiavelli M., Bertin G., Casertano S., Møller P., 2001, *MNRAS*, **326**, 237
- Treu T., Auger M. W., Koopmans L. V. E., Gavazzi R., Marshall P. J., Bolton A. S., 2010, *ApJ*, **709**, 1195
- Tu H., et al., 2009, *A&A*, **501**, 475
- Turner E. L., Ostriker J. P., Gott J. R. I., 1984, *ApJ*, **284**, 1
- Vegetti S., Koopmans L. V. E., Bolton A., Treu T., Gavazzi R., 2010, *MNRAS*, **408**, 1969
- Walsh D., Carswell R. F., Weymann R. J., 1979, *Nature*, **279**, 381
- Webster R., 1991, in Crampton D., ed., *Astronomical Society of the Pacific Conference Series Vol. 21, The Space Distribution of Quasars*. p. 160
- Windhorst R. A., et al., 2023, *AJ*, **165**, 13
- Wong K. C., et al., 2018, *ApJ*, **867**, 107
- Wong K. C., et al., 2020, *MNRAS*, **498**, 1420
- Wong K. C., Chan J. H. H., Chao D. C. Y., Jaelani A. T., Kayo I., Lee C.-H., More A., Oguri M., 2022, *PASJ*, **74**, 1209
- Wyithe J. S. B., Loeb A., 2002a, *Nature*, **417**, 923
- Wyithe J. S. B., Loeb A., 2002b, *ApJ*, **577**, 57
- Wyithe J. S. B., Turner E. L., Spergel D. N., 2001, *ApJ*, **555**, 504
- Wyithe J. S. B., Yan H., Windhorst R. A., Mao S., 2011, *Nature*, **469**, 181
- Zwicky F., 1937, *Physical Review*, **51**, 290
- de Vaucouleurs G., 1948, *Annales d'Astrophysique*, **11**, 247
- de Vaucouleurs G., 1953, *MNRAS*, **113**, 134
- van der Wel A., et al., 2014, *ApJ*, **792**, L6

This paper has been typeset from a $\text{\TeX}/\text{\LaTeX}$ file prepared by the author.